LUND UNIVERSITY

Atomistic investigation of the impact of phosphorus impurities on the tungsten grain boundary decohesion

Olsson, Pär; Hiremath, Praveenkumar; Melin, Solveig

Full length article

Atomistic investigation of the impact of phosphorus impurities on the tungsten grain boundary decohesion

Pär A.T. Olsson [a,b,*], Praveenkumar Hiremath [b], Solveig Melin [b]

[a] *Materials Science and Applied Mathematics, Malmö University, SE-205 06 Malmö, Sweden*
[b] *Division of Mechanics, Materials and Components, Lund University, Box 118, SE-221 00 Lund, Sweden*

ARTICLE INFO

ABSTRACT

In the present work, we have generated a new second-nearest neighbour modified embedded atom method potential (2NN-MEAM) for the W–P system to investigate the impact of P impurity segregation on the strength of symmetric ⟨110⟩ tilt coincident site lattice grain boundaries (GBs) in tungsten. By incorporating the impurity-induced reduction of the work of separation in the fitting strategy, we have produced a potential that predicts decohesion behaviour as found by *ab initio* density functional theory (DFT) modelling. Analysis of the GB work of separation and generalized stacking fault energy data derived from DFT and the 2NN-MEAM potential show that P-impurities reduce the resistance to both cleavage and slip. Mode I tensile simulations reveal that the most dominant mode of GB failure is cleavage and that pristine GBs, which are initially ductile, on most accounts change to brittle upon introduction of impurities. Such tendencies are in line with experimentally observed correlations between P-impurity content and reduced ductility.

1. Introduction

The emergence of tungsten (W) as one of the leading candidates for plasma-facing components in nuclear fusion reactors has triggered a surge to elucidate the inherent fracture mechanical properties of alloys with different grades and varying microstructures [1–3]. Among the concerns connected with using W-based alloys for such applications is the high brittle-to-ductile transition temperature (BDTT) [4,5], which lies in the range of 150–500 °C for polycrystals [5–11]. This poses a challenge for cooled components, such as divertor monoblocks with central water- or helium-cooled channels (see e.g. [12–14]), at which the thermal gradients are expected to produce significant tensile stress transients [14,15]. Such tensile stresses can be sufficiently high to cause brittle crack-propagation, which ultimately may jeopardize the integrity.

For polycrystalline W containing impurities, the joint interplay of microstructure (i.e. grain size distribution, dislocation density, texture, grain shapes, etc.) and impurity concentration dictate the emerging failure mechanisms [2]. The fracture resistance of grain boundaries (GBs) is generally lower than for transgranular cleavage, although microstructural constraints can promote the latter locally if the geometry of the GB and crack makes it unfavourable for intergranular fracture to ensue. Reported observations concerning the role of impurities on the embrittlement of W suggest that segregation of sulphur (S), oxygen (O) and phosphorus (P) at the GBs promotes reduced GB strength [4].

Especially P is believed to have a substantial effect on the GB embrittlement, as correlation between loss in ductility, which manifests in increasing portion of intergranular fracture, and increasing P content (>20–40 wppm) has been observed [16,17]. Below the concentration of 20–40 wppm it has been reported that P does not impact the fracture behaviour notably [2]. To gain further insight on the role of impurities on the GB strength of W, *ab initio* modelling based on density functional theory (DFT) has been employed to elucidate the impact on work of separation [18–26]. It has been reported that while P has an embrittling effect on $\Sigma3(111)[\bar{1}10]$, $\Sigma3(112)[\bar{1}10]$ and $\Sigma5(013)[100]$ GBs [18–22], for the $\Sigma27(552)[\bar{1}10]$ GB it promotes improved cohesion [18]. These findings suggest that the intrinsic properties of the GB govern whether P enhances or reduces the cohesion, which merits further investigation.

A limitation typically associated with DFT-based decohesion modelling is that the fracture plane often is prescribed on beforehand and dislocation nucleation is suppressed by the limited size of the supercell. To overcome such limitations, classical atomistic modelling, such as molecular dynamics (MD), can be used as it enables both temporal and spatial up-scaling. Although formally less accurate than DFT modelling, such strategies allow for both ductile and brittle mechanisms to ensue and there is no need to limit the fracture to predefined planes. For reliable predictions using MD, the utilized empirical potential needs to be constructed such that it reproduces the relevant fracture mechanical

properties. Typically, embedded atom method (EAM) [27,28] or modified embedded atom method (MEAM) potentials [29–31] are used for such modelling, but to the best of the authors' knowledge there are no interatomic potentials available for the W–P binary system.

The purpose of the present study is twofold: (i) to establish an interatomic potential for the W–P system with the capability to predict the change in strength for P inhabited GBs and (ii) to evaluate the impact of impurities for a set of ⟨110⟩ symmetric tilt coincident site lattice (CSL) GBs to provide insight on how P impurities affect the cohesion for GBs with different GB energies below the BDTT. For (i) we fit a new second nearest neighbour (2NN) MEAM potential to reproduce the embrittleing potency for GBs as computed by means of DFT. For (ii) we perform classical atomistic mode I tensile simulations of bicrystals with ⟨110⟩-symmetric tilt GBs (STGBs) that contain low concentrations of P impurities. Since the focus of the present study is on the behaviour below the BDTT, the simulations are performed at room temperature. For the considered GBs it is found that the peak stress is generally reduced by the presence of impurities and that several of the pristine GBs that behave in a ductile manner undergo a transition from plastic yielding to brittle cleavage as the impurity coverage increases.

The paper is outlined as follows: in the next section we give a brief overview of the 2NN-MEAM formalism and the herein utilized fitting strategy. This is followed by a description of the simulation setup for the decohesion modelling in Section 3. In the results (Section 4), we evaluate the performance of the binary potential and report the outcomes from the tensile simulations. Section 5 contains the discussion and finally in Section 6 the findings are summarized and the conclusions are stated.

2. Interatomic potential

2.1. 2NN-MEAM formalism

The theory behind the 2NN-MEAM formalism is thoroughly outlined in [32,33], here we only give a brief overview of the essentials. Within the MEAM framework, the total potential energy of an ensemble of particles is given as

$$E = \sum_i F_i(\bar{\rho}_i) + \sum_i \sum_{j \neq i} S_{ij} \phi_{ij}(r_{ij}) \tag{1}$$

where $F_i(\bar{\rho}_i) = A E_c (\bar{\rho}_i / \bar{\rho}_0) \ln(\bar{\rho}_i / \bar{\rho}_0)$ represents the embedding energy associated with immersing ion i into the background electron density $\bar{\rho}_i$, with E_c being the cohesive energy and $\bar{\rho}_0$ is the background electron density of the reference structure, while A is an adjustable parameter [33]. The function ϕ_{ij} is the pair interaction contribution between ions i and j, separated by the distance r_{ij} and S_{ij} is a screening function that moderates the second-nearest neighbour interaction.

There are different flavours of the 2NN-MEAM formalism. Following Baskes [34], the background electron density is computed by weighted superpositioning of a spherical $\rho_i^{(0)}$ and three angular dependent partial contributions, $\rho_i^{(1)} - \rho_i^{(3)}$, to the total electron density. They are constructed through spatial invariants and given as

$$\rho_i^{(0)} = \sum_{j \neq i} f_j^{(0)}(r_{ij}) \tag{2}$$

$$\rho_i^{(1)} = \left[\sum_{\alpha} \left[\sum_{j \neq i} f_j^{(1)}(r_{ij}) \frac{r_{ij}^{\alpha}}{r_{ij}} \right]^2 \right]^{1/2} \tag{3}$$

$$\rho_i^{(2)} = \left[\sum_{\alpha, \beta} \left[\sum_{j \neq i} f_j^{(2)}(r_{ij}) \frac{r_{ij}^{\alpha} r_{ij}^{\beta}}{r_{ij}^2} \right]^2 - \frac{1}{3} \left[\sum_{j \neq i} f_j^{(2)}(r_{ij}) \right]^2 \right]^{1/2} \tag{4}$$

$$\rho_i^{(3)} = \left[\sum_{\alpha, \beta, \gamma} \left[\sum_{j \neq i} f_j^{(3)}(r_{ij}) \frac{r_{ij}^{\alpha} r_{ij}^{\beta} r_{ij}^{\gamma}}{r_{ij}^3} \right]^2 \right]^{1/2} \tag{5}$$

where r_{ij}^{α} represents the individual components of the interatomic distance vector ($\alpha = x, y, z$). We emphasize that the herein utilized format

of Eq. (5) does not possess the nowadays commonly used orthogonal format introduced in [35]. The functions $f_j^{(h)}$ ($h = 0$–3) in Eqs. (2) to (5) are the pairwise electronic density functions given by

$$f_j^{(h)}(r_{ij}) = \rho_0 \exp[-\beta^{(h)}(r_{ij}/r_e - 1)] \tag{6}$$

for which ρ_0 and $\beta^{(h)}$ are fitting parameters and r_e is the nearest neighbour distance in the reference structure. In case of the binary potential, Eq. (6) is computed through standard averaging. The electron background density is given by

$$\bar{\rho}_i = \frac{2\rho_i^{(0)}}{1 + \exp[-\Gamma_i]} \tag{7}$$

where

$$\Gamma_i = \sum_{h=1}^{3} t^{(h)} [\rho_i^{(h)} / \rho_i^{(0)}]^2 \tag{8}$$

which contains three weight parameters, $t^{(h)}$, that regulate the relative contribution to the total background density.

The pairwise screening function S_{ij} in Eq. (1) is given by the product of the screening factors from all neighbouring particles, i.e.,

$$S_{ij} = \prod_{k \neq i, j} S_{ikj} \tag{9}$$

for which S_{ikj} is computed based on an elliptic geometry construction [32,33,36]. To illustrate the approach, for three particles (i, j and k) located in the xy-plane with the x-axis passing through the coordinates of particles i and j, an ellipse can be constructed as

$$x^2 + \frac{1}{C} y^2 = \left(\frac{1}{2} r_{ij} \right)^2 \tag{10}$$

where the C can be computed based on their relative positions. The screening of the pairwise potential and electron density contribution, S_{ikj}, between particles i and j due to k is found by establishing an inner ellipse, defined by C_{min}, within which all interaction is screened if it contains k. An outer perimeter ellipse, defined by C_{max}, is also constructed, beyond which no screening occurs. Then there is an intermediate elliptic region of partial screening between $C_{min} \leq C \leq C_{max}$. To this end, a screening function for the i, j, k-triplet is given by

$$S_{ikj} = f_c \left[\frac{C - C_{min}}{C_{max} - C_{min}} \right] \tag{11}$$

where f_c is the smooth function

$$f_c(x) = \begin{cases} 1 & x \geq 1 \\ (1 - (1 - x^4)^2)^2 & 0 \leq x < 1, \\ 0 & x \leq 0. \end{cases} \tag{12}$$

This yields two additional fitting parameters, C_{min} and C_{max}, for each elemental potential ($i - j - k$ = W–W–W and P–P–P) and eight for the mixed potential, i.e. ($i - j - k$ = W–P–W, P–W–P, W–W–P and W–P–P).

The pair potential, $\phi_{ij}(r_{ij})$, is determined by fitting the total energy to a variant of Rose's universal binding energy relation (UBER) [37,38],

$$E(a^*) = -E_c \left(1 + a^* + \frac{\alpha d a^{*3}}{a^* + \alpha} \right) \exp[-a^*] \tag{13}$$

where d is an adjustable parameter that can assume different values for $a^* < 0$ and $a^* > 0$, which is defined as $a^* = \alpha(r_{ij}/r_e - 1)$. The parameter α is given by $\alpha = \sqrt{9B\Omega/E_c}$ where B is the bulk modulus and Ω is the equilibrium atomic volume of the reference structure.

2.2. Elemental potentials

Although there are some thirty empirical interatomic potentials for W available in the literature (see e.g. the review by Bonny et al. [39]), to generate a potential for the W–P system we used our previously fitted elemental W [40] potential as starting point. The choice of
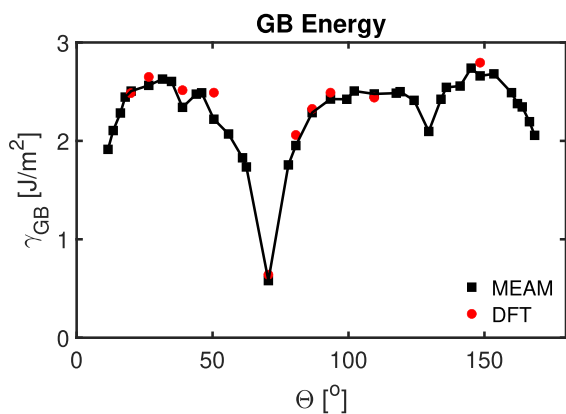
Fig. 1. Comparison of ⟨110⟩ STGB energy as function of the misorientation angle as predicted by the MEAM potential and DFT data [25].

	E_c	r_e	α	A	$\beta^{(0)}$	$\beta^{(1)}$	$\beta^{(2)}$	$\beta^{(3)}$
W	8.66	2.74	5.59	0.40	6.13	2.50	0.37	0.31
P	2.71	2.60	5.30	1.75	2.44	5.00	1.00	1.00
	$t^{(0)}$	$t^{(1)}$	$t^{(2)}$	$t^{(3)}$	C_{min}	C_{max}	$d(a^* > 0)$	$d(a^* < 0)$
W	1.00	2.38	0.33	−5.65	0.52	2.78	0.0	0.0
P	1.00	0.53	1.80	−1.01	1.42	2.80	0.0	0.0

this 2NN-MEAM potential over others available in the literature was motivated by the fact that it was fitted explicitly to reproduce surface energies of low-index surfaces as predicted by DFT, such that it quantitatively predicts Griffith's work of fracture. Moreover, it has been found to give a good representation of the generalized stacking fault energy curves, the unstable twinning energy and traction–separation behaviours, which makes it highly suitable to investigate small scale fracture mechanisms [40]. Moreover, evaluation of ⟨110⟩-symmetric tilt GBs, see Fig. 1, reveals a good agreement between the predicted GB energies, γ_{GB}, of the MEAM potential and results from DFT modelling [25], which demonstrates the W potential's strong capability to reproduce realistic energies for pristine GBs.

Pure P exists in several different allotropes, including white, red and black phosphorus, for which the bonding comprises both covalent and long-range van der Waals interaction. Although van der Waals interaction is important to describe the interaction in pure P [41,42], its impact on the bonding when dissolved in metals becomes much less important than angular and metallic bonding components. Thus, for the present scope, as an approximation we neglected van der Waals interaction and instead focused on incorporating the directional and metallic components in the model through the MEAM formalism.

There are two available elemental 2NN-MEAM potentials for P published in the literature, which were derived as part of binary Fe–P [43] and Si–P [44] potentials. In terms of performance, the latter has shown a broader predictability of the P-phases, but since $\beta^{(2)}$ and $\beta^{(3)}$ of Eq. (6) were negative, the contribution to the background density increased with increasing separation up to the point at which the smooth cutoff was activated. In light of this unusual behaviour, we opted to use the P potential from [43] as starting point for our fitting. Because the original P potential was fitted using mainly an ultrasoft pseudopotential setup, while we used projector augmented wave (PAW) pseudopotentials (see Appendix A), and because it was fitted to another expression for the partial contribution to the electron background density, $\rho_i^{(3)}$ (Eq. (5)), we made some minor edits to retain much of the properties that were predicted by the original potential, see Table 1. In connection with this refitting we did an evaluation of several of the properties reported in [43] and found only what we consider to be minor differences. We note that the P potential uses the body-centred cubic (BCC) lattice as reference and the parameters for both elemental potentials are given in Table 1. In accordance with [45], we chose the cutoff and smoothing distances to be large, i.e. $r_c = 5.8$ Å and $\Delta r = 2.5$ Å, to prevent artificial blunting behaviour.

2.3. Binary potential fitting and evaluation strategy

The binary potential was fitted using an optimization scheme for which we adopted a simplex search algorithm [46] to minimize the weighted objective function that contained the target properties, i.e.,

$$G(\mathbf{x}) = \sum_{i=1}^{N} w_i |y_i - g_i(\mathbf{x})| \tag{14}$$

where w_i represents the weight, y_i is the target property and $g_i(\mathbf{x})$ is the prediction by the 2NN-MEAM potential. To avoid overfitting the potential and thus limit the predictability, we established separate fitting and evaluation databases, for which the majority of the data emanated from DFT modelling conducted herein. For details about the DFT modelling, see Appendix A.

There is a number of tungsten phosphides with varying stoichiometry, including WP and WP_2, along with the metastable WP_4 phase and a couple of phases whose stability is subject to debate, i.e. W_2P and W_3P_4 [47,48]. But the ground state crystal structures of those were too complex to be used as reference for the 2NN-MEAM cross-potential. Because the purpose of the present potential was to capture the grain boundary strength of tungsten containing only dilute amounts phosphorus, instead we used the hypothetical $L1_2$-W_3P structure as reference, whose energy–volume curve was used as part of the fitting database. In addition, we fitted the potential to reproduce the energy–volume curves of the fictitious B2-WP (CsCl), B3-WP (zincblende) and B4-WP (wurtzite) crystals and the bulk substitutional formation energy as derived by means of DFT.

The utilized elemental W potential is known to reproduce both the work of separation and traction–separation behaviour of bulk and pristine GBs [40]. To capture the impact of impurities on the traction–separation behaviour, as part of the fitting database we used the rigid work of separation as derived by DFT for the $\Sigma3(112)[1\bar{1}0]$ GB containing P impurities. This low energy twin boundary is frequently occurring in the tungsten BCC phase, which makes it relevant for the predictability of the potential. For this purpose we considered a GB containing P-substitutionals equivalent to the impurity coverage $\theta = 0.02$ Å^{-2} (defined as the number of impurities per area-unit of the interface). They were ideally positioned and relaxed at high symmetry sites in the centre of the GB, as indicated in Fig. 2(a), whereafter the GB was ideally cleaved such that the rigid work of separation could be extracted.

Regarding the point defect energies, we note that the pure W potential predicts the ⟨110⟩ split dumbbell as the ground state self-interstitial configuration [40], whereas DFT modelling has demonstrated the ⟨111⟩ split dumbbell to be the ground state [49,50]. This has been commonly observed for other 2NN-MEAM BCC potentials as well [33], which suggests that interstitial configurations (self and foreign) were not captured by default. Thus, instead of incorporating interstitial configurations in the fit, we focused on fitting the potential to reproduce the formation energy of bulk substitutionals, which through DFT modelling has been predicted to be the most stable solute configuration for P in W [51].

In addition to the fitting database, to investigate the performance of the potential we evaluated its predictability in terms of energy–volume curves of the fictitious B1-WP (rocksalt) and C1-W_2P (fluorite) structures. Moreover, the work of separation and traction–separation curves were evaluated for $\Sigma3(112)[1\bar{1}0]$ and $\Sigma5(310)[001]$ GBs containing either substitutionals or interstitials. For this evaluation the P impurities were purposely positioned at high symmetry sites in the centre of the GBs,
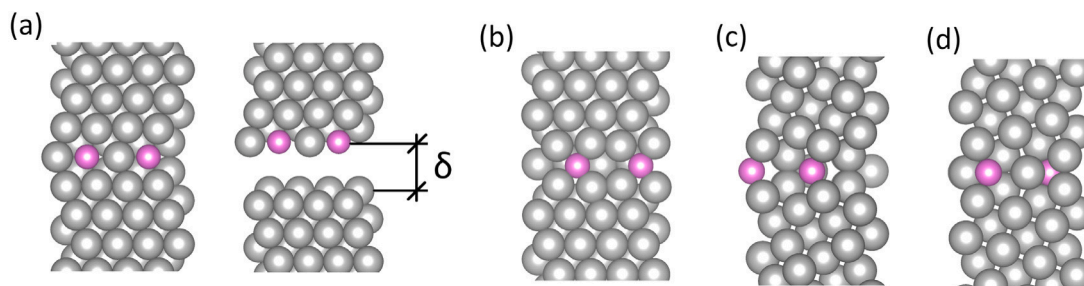
Fig. 2. Illustration of (a, b) $\Sigma3(112)[1\bar{1}0]$ and (c, d) $\Sigma5(310)[001]$ CSL symmetric tilt GBs containing P-impurities as (a, c) substitutionals and (b, d) interstitials. In (a) we schematically illustrate the RGS modelling approach, which was used for generating potential fitting and validation data.

see Fig. 2(b)–(d), so that the potential's ability to predict the cohesion for both high and low energy GBs, with different occupied impurity segregation sites, could be tested. To this end, we adopted the rigid grain shift (RGS) method, see e.g. [52], such that no atomic relaxations were involved in the traction–separation curve generation, see Fig. 2(a). Although atomic relaxation is necessary for an accurate description of the traction–separation properties, it gives rise to a non-unique traction–separation curve whose peak stress and critical separation are dependent on the number of layers in the model [53–55], which is not an issue for the RGS approach due to the localized deformation. Also for the fitting and evaluation of the binary potential the RGS approach was beneficial as it gave a more straightforward evaluation procedure and a consistent description of the forces across the interface, such that the impact of impurities on the interfacial strength could be incorporated. For the evaluation procedure we considered GBs that contained impurity coverages up to $\theta = 0.04$ Å^{-2}.

To assess the potential's predictability in terms of slip behaviour, we evaluated the generalized stacking fault energy (GSFE) profiles associated with the $\{110\}\langle111\rangle$ and $\{112\}\langle111\rangle$ slip systems against that of DFT. To produce relaxed GSFE curves, supercells comprising 12 $\{110\}$ and 18 $\{112\}$ layers, respectively, were generated and incrementally sheared at the periodic boundary until the total distance of glide was equal to the perfect Burgers vector, $(a/2)\langle111\rangle$. For each increment, the atoms were allowed to relax in the normal-direction of the slip plane only. To probe the impact of impurities we considered both pristine slip interfaces and those containing substitutionals up to the impurity coverage $\theta \sim 0.02$ Å^{-2}.

3. Intergranular decohesion modelling

In order to gain insight into the embrittleing effects of P impurities segregated at GBs, we investigated the tensile behaviour of $\langle110\rangle$ STGBs containing impurities. The considered coverage was up to $\theta = 0.02$ Å^{-2}. Under the assumption that all P atoms exclusively segregate at the GBs, this translates to ~ 8 wppm P impurity concentration for grains with an average ~ 4.4 μm diameter, which is of the order of the impurity concentration typically observed experimentally [2]. The details of the STGBs studied here are provided in Table 2.

The atomistic geometries were generated through a multi-step procedure, where we first generated pristine GBs using the open source GB code [57] and identified the ground state through the usage of the γ-surface approach, see e.g. [25]. To obtain an initial impurity distribution, the element type of randomly chosen atoms in the GB proximity were exchanged, such that a Gaussian impurity concentration profile that matches the target coverage was obtained. The equilibrium distribution of interfacial P atoms was determined by using hybrid Monte Carlo (MC) and MD simulations [58]. In the MC part of the simulation, W atoms were swapped with P atoms using the Metropolis criterion [59–62]. While the MD simulations were performed at 300 K in the isobaric–isothermal (NPT) ensemble, because the impurities did not always segregate at low energy sites sufficiently fast, we increased the temperature to $T = 2000$ K to enable a higher acceptance rate

Table 2
Details of the herein considered $\langle110\rangle$ STGBs. Here, Σ is the coincidence site lattice density, (klm) is the boundary plane and Θ is the misorientation angle in degrees. The parameters p and q are the prime integers that satisfy $\Sigma = (p^2 + 2q^2)/2$ and $\Theta = (2\arctan(\sqrt{2} \cdot q/p))$ [56].

Σ	(klm)	p	q	Θ	Σ	(klm)	p	q	Θ
99	$(\bar{7}7\bar{1})$	14	1	11.54	17	$(3\bar{3}\bar{4})$	4	3	93.37
73	$(6\bar{6}1)$	12	1	13.44	43	$(5\bar{5}\bar{6})$	6	5	99.37
51	$(5\bar{5}1)$	10	1	16.10	81	$(\bar{7}78)$	8	7	102.12
83	$(11\bar{9})$	9	1	17.86	3	$(1\bar{1}\bar{1})$	1	1	109.47
33	$(4\bar{4}1)$	8	1	20.05	67	$(\bar{7}76)$	6	7	117.56
19	$(\bar{1}16)$	6	1	26.53	97	$(66\bar{5})$	5	6	118.98
27	$(\bar{1}15)$	5	1	31.59	41	$(4\bar{4}\bar{3})$	3	4	124.12
89	$(\bar{2}29)$	9	2	34.89	11	$(\bar{3}32)$	2	3	129.52
9	$(\bar{1}14)$	4	1	38.94	59	$(33\bar{1}0)$	3	5	134.02
57	$(\bar{2}27)$	7	2	44.00	57	$(\bar{7}74)$	4	7	135.99
59	$(5\bar{5}3)$	10	3	45.98	9	$(2\bar{2}\bar{1})$	1	2	141.06
11	$(\bar{1}13)$	3	1	50.48	89	$(9\bar{9}\bar{4})$	4	9	145.11
41	$(\bar{3}38)$	8	3	55.88	27	$(\bar{5}52)$	2	5	148.41
97	$(5\bar{5}12)$	12	5	61.02	19	$(\bar{3}31)$	1	3	153.48
67	$(\bar{3}37)$	7	3	62.44	33	$(\bar{1}1\bar{8})$	1	4	159.95
3	$(\bar{1}12)$	2	1	70.53	83	$(9\bar{9}\bar{2})$	2	9	162.14
81	$(4\bar{4}7)$	7	4	77.89	51	$(\bar{1}1\bar{1}0)$	1	5	163.90
43	$(\bar{3}35)$	5	3	80.63	73	$(1\bar{1}\bar{1}2)$	1	6	166.56
17	$(2\bar{2}\bar{3})$	3	2	86.63	99	$(1\bar{1}\bar{1}4)$	1	7	168.46

when evaluating the Metropolis criterion. On most accounts the resulting ground state energies and impurity concentration profiles of the generated configurations were similar regardless of the MC swapping temperature, but in the case of GBs containing $\langle100\rangle$-dislocations we found that the impurities did not segregate properly at the lowest energy sites within the dislocation cores unless the temperature was increased. This required us to increase the temperature for the MC part such that configurations with lower ground state energy could be obtained. These hybrid simulations ran for a total of 200 ps with a timestep of 1 fs, which was followed by additional equilibration at room temperature under NPT conditions to obtain fully equilibrated configurations.

For the tensile simulations, the orientation of the STGBs was chosen such that the rotation-axis of GBs was parallel to the y−direction and the z-axis coincided with the GB normal direction, see Fig. 3. The effects of free surfaces were avoided by using a simulation cell that was periodic in all directions, while maintaining a minimum separation of 75 Å between neighbouring GBs, which ensured that no interaction occurred between them along the z−direction. With the in-plane dimensions of the setup being ~45 Å × 45 Å, constrained boundary conditions that corresponded to zero lateral strain [63–69] were applied in the in-plane directions, i.e. $\epsilon_{xx} = \epsilon_{yy} = 0$. For the GBs that showed any degree of plasticity, the lateral dimensions were also increased to ~150 Å × 150 Å to eliminate any in-plane finite size dependency. To effectuate the loading, the samples were subjected to a constant engineering strain rate in the z−direction, which was converged with respect to the stress–strain curves. It was found that $\dot{\epsilon} = 1 \cdot 10^8$ s^{-1} was sufficient to yield converged results. Throughout the
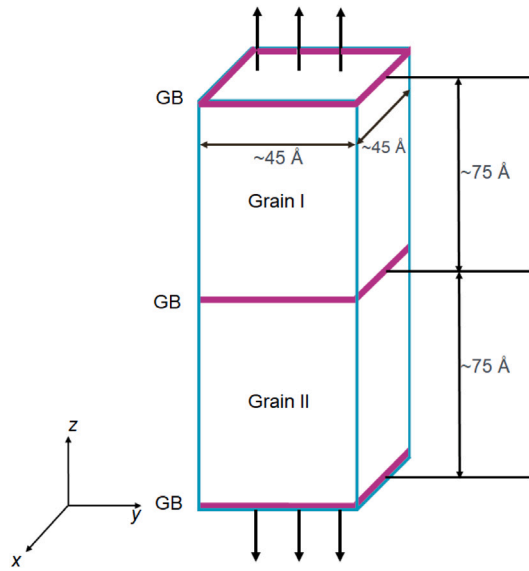
Fig. 3. Schematic of the utilized 3D-STGB tensile simulation setup.

Table 3

2NN MEAM potential parameters of for the binary W–P and potential. Here, r_e and E_c, are in Å and eV units, respectively. The remaining parameters are unitless.

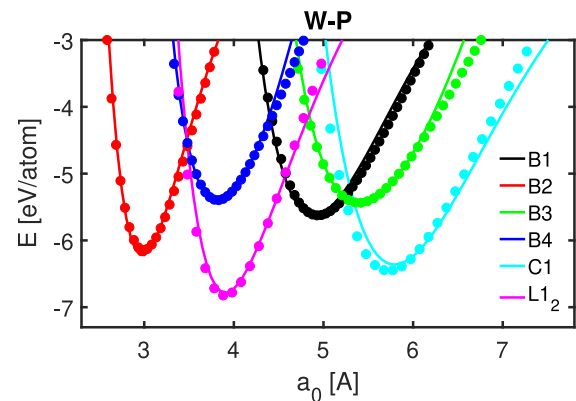|	W–P
Reference structure	L1$_2$-W$_3$P
r_e	2.762
E_c	6.787
α	5.912
$\rho^W : \rho^P$	1:0.718
C_{max}(W–P–W)	3.141
C_{max}(P–W–P)	2.000
C_{max}(W–W–P)	2.643
C_{max}(P–P–W)	2.758
C_{min}(W–P–W)	0.336
C_{min}(P–W–P)	1.000
C_{min}(W–W–P)	0.500
C_{min}(P–P–W)	1.487
$d(a^* > 0)$	0.040
$d(a^* < 0)$	0.000

Fig. 4. Energy–volume profiles for the B1, B2, B3, B4, C1 and L1$_2$ phases for the W–P potential. The solid lines correspond to 2NN-MEAM predictions, whereas the markers are herein generated DFT data.

simulations the temperature was maintained at the target temperature through the employment of a Nosé–Hoover thermostat [70–73]. The engineering stress tensor was computed from the virial stress [74,75] as

$$\sigma^{\alpha\beta} = -\frac{1}{V_0} \sum_{i=1}^{n} \left[m_i v_i^\alpha v_i^\beta + \sum_{j<i}^{n} F_{ij}^\alpha r_{ij}^\beta \right] \qquad (15)$$

where F_{ij}^α is the force acting between the ith and jth-atoms, while m_i and v_i^α denote the atomic mass and velocity vector, respectively, and V_0 is the initial cell volume.

The adopted uniaxial-strain controlled setup that utilizes periodic lateral boundaries with prescribed zero strain has been extensively used for previous GB mode I tensile modelling, see e.g. [63–69]. Although the periodic boundaries restrict dislocation nucleation, the prescribed zero lateral strains reflect the multiaxial stress state that is expected to emerge at crack-tips under plane strain loading, or as a result of microstructural constraints imposed by the neighbouring grains, GBs or triple junctions. This makes it a suitable setup for modelling the impact of impurities on the mode I GB decohesion.

4. Results

4.1. Evaluation of binary potential

In the current section we evaluate the fitted binary potential. The resulting potential parameters are compiled in Table 3 and potential files for usage in LAMMPS [76,77] are available as part of the supplementary material.

4.1.1. Defect and bulk phase properties

The substitutional defect energy was computed by means of fully relaxed DFT modelling (see Appendix A) and used for the fit. It was found to correspond to 0.68 eV, which concurs with the corresponding DFT data, which was found to be 0.67 eV. Even though no effort was made to fit the potential to reproduce the bulk interstitial configurations, three different meta-stable configurations were observed: $\langle 100 \rangle$, $\langle 110 \rangle$ and $\langle 111 \rangle$ split dumbbells. The respective formation energies were 6.88, 5.38 and 5.61 eV. Compared with DFT data (i.e. 4.81, 5.50 and 5.78 eV, respectively), especially the formation energy associated with the $\langle 100 \rangle$ interstitial deviates, whereas the others agree well. Thus,

much like for the elemental W potential, the binary potential does not predict the accurate formation energy order of different bulk interstitial configurations.

The energy–volume curves for the cubic B1–B3, C1 and L1$_2$ phases are given in Fig. 4 along with the corresponding curves as derived from DFT. Moreover, the curve for the hexagonal wurtzite B4 phase is given for the ideal lattice parameter ratio $c/a = \sqrt{8/3}$. It is found that the potential captures most of the characteristic features of the DFT data in the proximity of the energy minima. This is especially true for the B2–B4 and L1$_2$ lattices, which were included in the fitting database. But also the other phases were found to agree well with the DFT data. At most the deviation of the equilibrium lattice parameter is 0.06 Å between the MEAM and DFT, and the energy minima are within 0.1 eV/atom, indicating good transferability.

4.1.2. Traction–separation properties and generalized stacking fault energy

The energy- and traction–separation curves as computed by means of DFT and the generated potential can be seen in Fig. 5. Owing to the fact that the work of separation for the $\Sigma 3(112)[1\bar{1}0]$ GB with a substitutional impurity coverage of $\theta = 0.02$ Å^{-2} was included in the fitting database, not surprisingly, the potential is found to realistically reproduce such behaviour, see Fig. 5(a). The work of separation deviates by less than 10% compared to DFT data for all concentrations. The predicted peak stresses are within 0.5 GPa of that computed by means of DFT, which corresponds to less than 2% deviation. Likewise, the critical separation, at which the peak stress occurs, deviates by less than 0.1 Å, see Fig. 5(b). For the same GB containing interstitials, we similarly find good agreement between the classical potential and DFT,
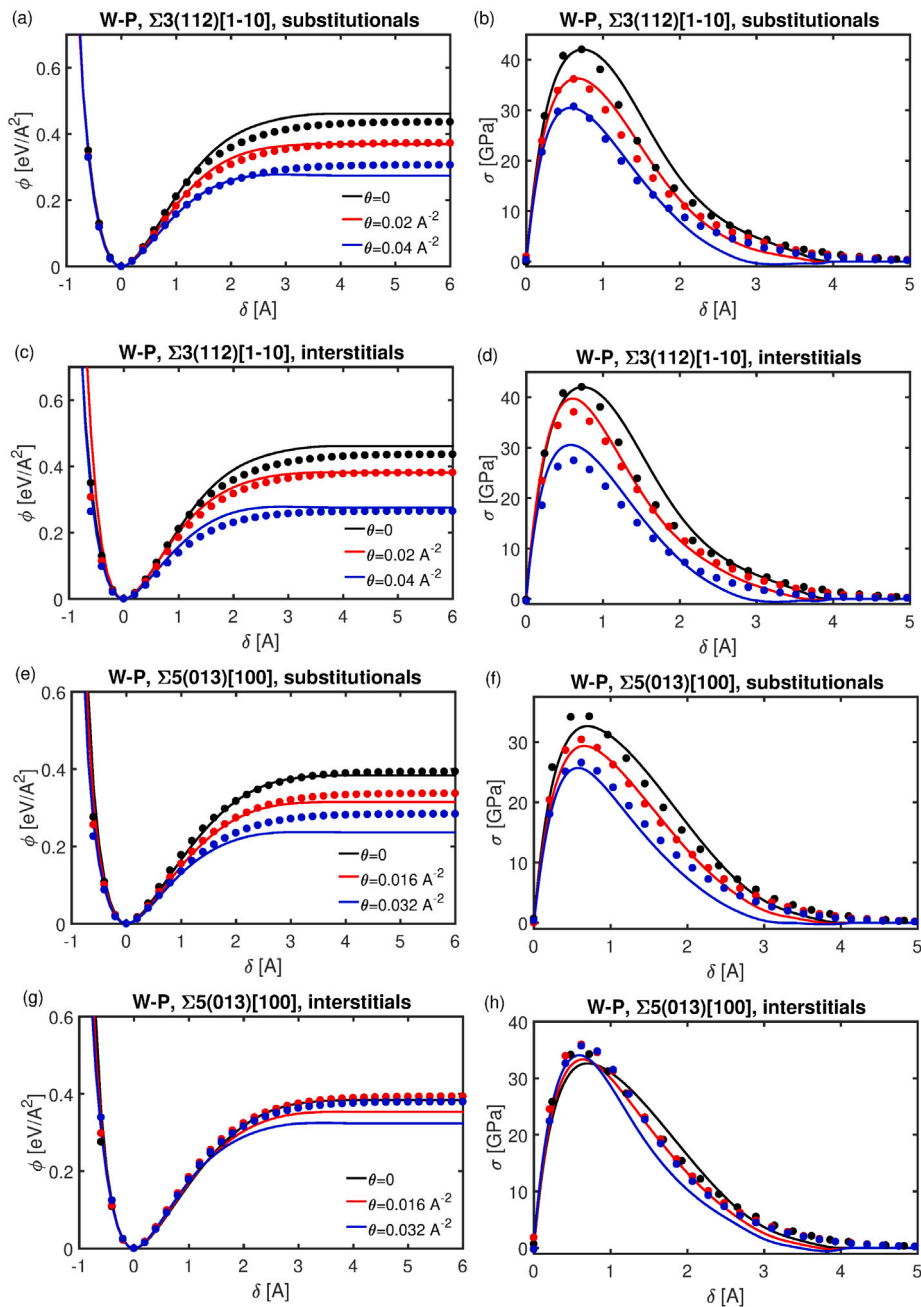
Fig. 5. Energy–separation and traction–separation curves for (a–d) $\Sigma 3(112)[1\bar{1}0]$ and (e–h) $\Sigma 5(013)[100]$ CSL symmetric tilt GBs containing P impurities: (a, b, e, f) substitutionals and (c, d, g, h) interstitials. The left panel represent energy–separation curves and the right panel comprises traction–separation curves. The solid lines correspond to 2NN-MEAM predictions, whereas the markers are herein generated DFT data.

see Fig. 5(c, d). The work of separation are in excellent agreement, with deviations less than 0.01 eV/Å^2, while the peak stresses are within 2 GPa of that predicted by DFT.

Even though they were not included in the fit, we obtain good agreement for the $\Sigma 5$ GB with substitutionals, see Fig. 5(e, f). Despite being slightly overestimated, the peak stresses are within 3 GPa (i.e. ~10%) and the work of separation is within 0.04 eV/Å^2 (i.e. ~10%) of those predicted by DFT. For the $\Sigma 5$ GB containing interstitials, we note that DFT and the empirical potential both indicate that the P impurities do not have any substantial effect on the GB peak stress and work of separation, see Fig. 5(g, h). This is in contrast to our previous findings [22], where significant reductions in the peak stress and work of separation were found. This discrepancy is likely due to the fact that atomic relaxations were allowed in [22], while they

were prevented for the validation herein — both for the DFT and classical modelling. In fact, for iron and nickel GBs it has been found that rigid and relaxed GB separation modelling can give contradictory results and that atomic relaxation is necessary to quantitatively capture the impact of impurities on the GB strength [52,78]. Nevertheless, as for the previously mentioned cases, the peak stresses for impurity inhabited GBs are within 10% of those predicted by DFT, suggesting good predictability.

Concerning slip mechanisms we compare the impact of impurities on the GSFE behaviour of the $\{110\}\langle 111 \rangle$ and $\{112\}\langle 111 \rangle$ slip systems using the 2NN-MEAM potential and DFT, see Fig. 6. It is found that the impurities contribute to a reduced threshold, which matches the results from DFT. For the former slip system it is found that the tendencies predicted by DFT are captured by the empirical potential. For the GSFE
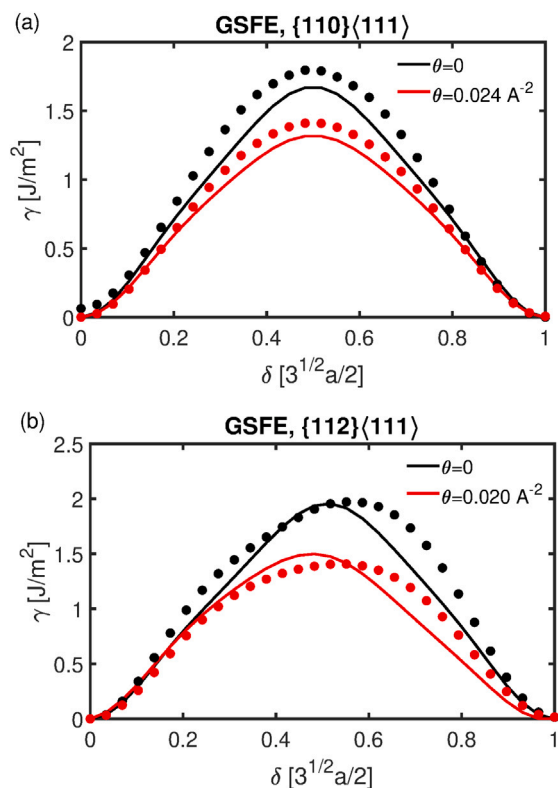
Fig. 6. Generalized stacking fault energy profiles associated with (a) the {110}⟨111⟩ and (b) {112}⟨111⟩ slip systems with and without impurities. The solid lines correspond to 2NN-MEAM predictions, whereas the markers are herein generated DFT data.

Fig. 7. Fracture surfaces for the $\Sigma 43(\bar{3}35)[110]$ GB indicating (a) faceting for the pristine GB and (b) lack thereof for the impurity coverage $\theta = 0.02$ Å^{-2}.

Fig. 8. DTVB failure events in as observed in the pristine $\Sigma 41(\bar{3}38)[110]$ GB. (a) Dislocation and twin nucleation, (b) void formation and (c) cleavage.

associated with {112}⟨111⟩ slip, we note that the peak of the GSFE curve derived from DFT is slightly perturbed to an off-centre position, which is in accordance with previous DFT results in [40,79]. Although our potential does not produce such significant asymmetric profile, the peak energies of the potential match the DFT data well, which suggests that even though the binary potential was not explicitly fitted for it, it captures the impact of impurities on slip resistance.

Owing to the consistency between the DFT and classical results, the potential seems to quantitatively capture the impact of impurities on the plastic mechanisms and GB cohesion, which are strong indicators that it is appropriate for modelling GB failure and P-induced GB embrittlement.

4.2. Grain boundary tensile behaviour

The response of GBs subjected to the aforementioned deformation-controlled tensile setup using classical MD modelling is presented in this section. Emphasis is on the different failure mechanisms, brittle stress–strain and peak stress behaviour for the pristine GBs and those containing P impurities.

4.2.1. Failure mechanisms

From Table 4, it is apparent that intergranular brittle fracture is the dominant mode of failure in both pristine and P inhabited GBs. The brittle behaviour can be categorized primarily into two subcategories, henceforth referred to as B and B$_{\{110\}}$, respectively. The GBs belonging to the former undergo intergranular cleavage at the interfacial plane, whereas for the latter the cleavage is accompanied by the formation of {110}-facets along the interface, as shown in Fig. 7(a). This surface has the lowest surface energy [40], and it is found that increasing the P coverage on most accounts do not affect the faceting. But on rare instances is it noted that the facets on the fractured surfaces are locally
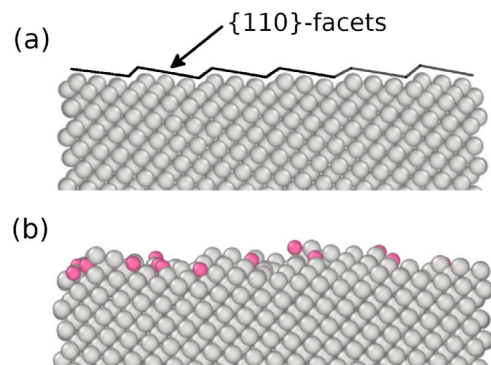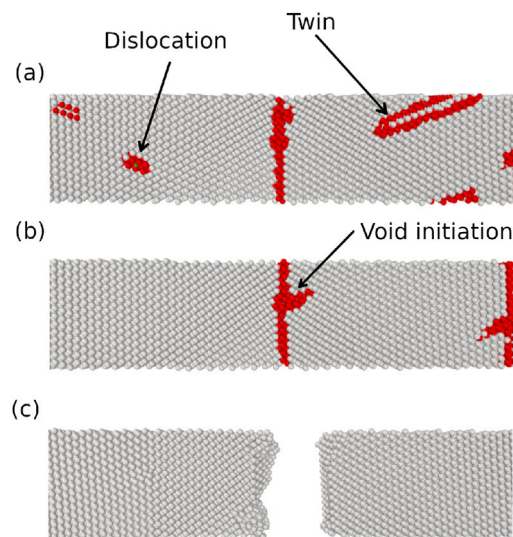
disrupted following introduction of P, see Table 4 and Fig. 7(b). It is further noted that the fractured surfaces are typically decorated with exposed P atoms, which is an indication that the cleavage generally propagates through paths that are interconnected via P impurities located in the GB proximity.

Limited plasticity is observed among the W GBs — only three of the pristine medium angle (MA) GBs with 44° < Θ < 153° show plasticity in the form of dislocation nucleation followed by twinning and the formation of voids before ultimately leading to brittle failure (referred to as DTVB), see Fig. 8. By gradually increasing the P impurity coverage in these GBs, the initially occurring plastic mechanisms are eventually suppressed for the benefit of brittle failure. But it is noted that the required amount of impurities to achieve such change in mechanism varies for the different GBs.

Three of the low-angle (LA) GBs (with Θ < 44°) and one high-angle (HA) GB (with Θ > 153°) undergo brittle failure that is preceded by twin and void formation, see Table 4. But similar to the MAGBs, when the P impurity coverage increases to 0.02 Å^{-2}, the failure mechanisms changes from ductile to pure cleavage without prior twinning or void formation.

Following coordinate relaxation, most of the LA and HAGBs harbour dislocations at the GB interface. Analysis based on the dislocation extraction algorithm (DXA [80], as implemented in the OVITO software [81]) reveals that the observed dislocations are either of $\frac{a}{2}\langle 111\rangle$ or $a\langle 100\rangle$ type. When introducing P atoms, they preferentially segregate

Computational Materials Science 219 (2023) 112017

Table 4
Failure mechanisms for $\langle 110 \rangle$ STGBs subjected to tensile loading. Here, B is clean brittle failure, while $B^{\langle 100 \rangle}$ represents brittle failure of GBs whose ground states are inhabited by $a\langle 100 \rangle$-type dislocations. Subscript is used whenever facetting at the cleaving interface was observed. "TVB" is used for observed twin and void formation preceding brittle failure, while the designation $DB^{\langle 111 \rangle}$ is used for GBs that contain $(a/2)\langle 111 \rangle$-type dislocations and undergo initial plastic behaviour before brittle failure ensues. DTVB represents brittle behaviour preceded by dislocation nucleation, twin and void growth.

Σ	Θ	$\theta = 0.0$ Å^{-2}	$\theta = 0.01$ Å^{-2}	$\theta = 0.02$ Å^{-2}	Σ	Θ	$\theta = 0.0$ Å^{-2}	$\theta = 0.01$ Å^{-2}	$\theta = 0.02$ Å^{-2}
99	11.54	$DB^{\langle 111 \rangle}$	$DB^{\langle 111 \rangle}$	$DB^{\langle 111 \rangle}$	17	93.37	B	B	B
73	13.44	$DB^{\langle 111 \rangle}$	$DB^{\langle 111 \rangle}$	$DB^{\langle 111 \rangle}$	43	99.37	B	B	B
51	16.10	$DB^{\langle 111 \rangle}$	$DB^{\langle 111 \rangle}$	$DB^{\langle 111 \rangle}$	81	102.12	B	B	B
83	17.86	$B^{\langle 100 \rangle}$	$B^{\langle 100 \rangle}$	$B^{\langle 100 \rangle}$	3	109.47	B	B	B
33	20.05	$DB^{\langle 111 \rangle}$	$DB^{\langle 111 \rangle}$	$DB^{\langle 111 \rangle}$	67	117.56	B	B	B
19	26.53	$B^{\langle 100 \rangle}$	$B^{\langle 100 \rangle}$	$B^{\langle 100 \rangle}$	97	118.98	B	B	B
27	31.59	TVB	TVB	B	41	124.12	B	B	B
89	34.89	TVB	TVB	B	11	129.52	B	B	B
9	38.94	TVB	TVB	B	59	134.02	B	B	B
57	44.00	B	B	B	57	135.99	B	B	B
59	45.98	B	B	B	9	141.06	$B_{\{110\}}$	$B_{\{110\}}$	$B_{\{110\}}$
11	50.48	B	B	B	89	145.11	$B_{\{110\}}$	$B_{\{110\}}$	$B_{\{110\}}$
41	55.88	DTVB	DB	B	27	148.41	B	B	B
97	61.02	DTVB	DVB	DB	19	153.48	$B^{\langle 100 \rangle}_{\{110\}}$	$B^{\langle 100 \rangle}_{\{110\}}$	$B^{\langle 100 \rangle}_{\{110\}}$
67	62.44	DTVB	DVB	B	33	159.95	$B^{\langle 100 \rangle}_{\{110\}}$	$B^{\langle 100 \rangle}$	$B^{\langle 100 \rangle}$
3	70.53	B	B	B	83	162.14	$DB^{\langle 111 \rangle}$	$DB^{\langle 111 \rangle}$	$DB^{\langle 111 \rangle}$
81	77.89	B	B	B	51	163.90	$B^{\langle 100 \rangle}$	$B^{\langle 100 \rangle}$	$B^{\langle 100 \rangle}$
43	80.63	$B_{\{110\}}$	$B_{\{110\}}$	B	73	166.56	$B^{\langle 100 \rangle}$	$B^{\langle 100 \rangle}$	$B^{\langle 100 \rangle}$
17	86.63	$B_{\{110\}}$	B	B	99	168.46	$DTVB^{\langle 100 \rangle}$	$B^{\langle 100 \rangle}$	$B^{\langle 100 \rangle}$
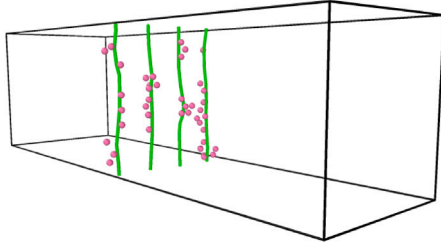
Fig. 9. Segregated impurities at $a/2\langle 111 \rangle$-dislocation cores located at a GB. The green lines indicate the dislocation lines and the purple particles are P-atoms, while the W-atoms have been filtered out.

close to the core of the dislocations located at the GB interface, see Fig. 9.

The $\frac{a}{2}\langle 111 \rangle$ dislocations are found to be mobile upon loading, which results in plastic behaviour prior to the brittle failure. Such response to the loading is represented by $DB^{\langle 111 \rangle}$ in Table 4. The introduction of impurities does not affect the observed events of failure mechanisms.

The GBs containing $a\langle 100 \rangle$ dislocations do not undergo any such plastic behaviour since the dislocations are confined to the GB interface at all times (referred to as $B^{\langle 100 \rangle}$, or $B^{\langle 100 \rangle}_{\{110\}}$ when faceting occurred, see Table 4). Their lack of mobility is attributed to the previously observed high unstable stacking fault energy barrier associated with displacements along the $a\langle 100 \rangle$ Burgers vector [82,83]. However, on one occasion (the pristine $\Sigma99(1\bar{1}14)[110]$ GB, see Table 4) do we observe ductile behaviour, but for that case it is not the movement of the $a\langle 100 \rangle$ dislocations, it is rather the nucleation of $\frac{a}{2}\langle 111 \rangle$ dislocations that precedes twinning and void formation before ultimately leading up to brittle failure. Similar to the $\frac{a}{2}\langle 111 \rangle$ dislocations, impurities preferentially segregate at the cores of the $a\langle 100 \rangle$ dislocations. But it is not clear if segregated impurities at the dislocation cores have any impact on the dislocation mobility, since the observed fracture behaviour is consistently brittle for such GBs.

4.2.2. Impurity-induced grain boundary weakening

To probe the influence of P impurities on the GB decohesion properties, we study the dependence of the brittle stress–strain behaviour on θ, with emphasis on the peak stress, $\sigma_{T,peak}$. Thus, we focus on GBs that undergo brittle failure, i.e. B, $B_{\{110\}}$, $B^{\langle 100 \rangle}$ and $B^{\langle 100 \rangle}_{\{110\}}$, see Table 4. The stress–strain curves for all of these failure modes are similar and

illustrated for the $\Sigma27(552)[1\bar{1}0]$ GB in Fig. 10(a) for varying values of θ. Since most of the elastic energy is stored within the grains, the initial elastic response is not affected by the presence of P impurities such that the stress–strain curves overlap for the initial stages of strain. However, the critical strain, which coincides with the peak stress, reduces with increasing impurity content, which in turn leads to reduced $\sigma_{T,peak}$ (see Fig. 10(b)). Thus, a trend of decreasing peak stress with increasing coverage of P atoms is obtained, which highlights their embritteling effect on GBs.

Motivated by the Griffith theory [84], which relates the energy release rate, G_{IC}, with the fracture stress of brittle solids,

$$\sigma_{T,peak} \propto \sqrt{G_{IC}} \tag{16}$$

we investigate how the peak stress varies with the idealized energy release rate $G_{IC} = 2\gamma_S - \gamma_{GB}$, where γ_S is the ideal surface energy of the created surfaces as calculated using the MEAM potential at $T = 0$ K. We note that this temperature deviates from that in our MD simulations, which were performed at 300 K. But since previous DFT works have demonstrated that the thermally-induced reductions of γ_S and γ_{GB} at room temperature compared to those at absolute zero temperature are generally less than $\sim 10\%$ [85], the thermal impact on γ_S and γ_{GB} are expected to be small for this relatively minor temperature difference. Thus, the zero temperature data is anticipated to be representative for the energy release rate.

On average, it is seen that the reduction in peak stress for the considered GBs corresponds to ~ 4.5 GPa when increasing the impurity coverage from $\theta = 0$ to 0.02 Å^{-2}, see Fig. 10(c). However, the decrease varies significantly among the GBs and the maximum decrease is observed for the $\Sigma3(112)[1\bar{1}0]$ twin GB, for which $\sigma_{T,peak}$ reduces by ~ 10 GPa. The standard deviation associated with the fit ranges from 1.53 GPa for $\theta = 0.02$ Å^{-2} to 2.67 GPa for $\theta = 0$, which suggests that the linear fit to (16) provides a rough estimate at best. The lack of correlation is connected to the fact that the cleavage is not necessarily ideal and does not occur at the same fracture plane throughout the separation process.

5. Discussion

Owing to phosphorus being virtually insoluble in tungsten, it is known to contain only low concentrations of P, which typically segregates at the GBs [2]. To generate an empirical potential suitable for modelling impurity induced GB embrittlement, we have adopted
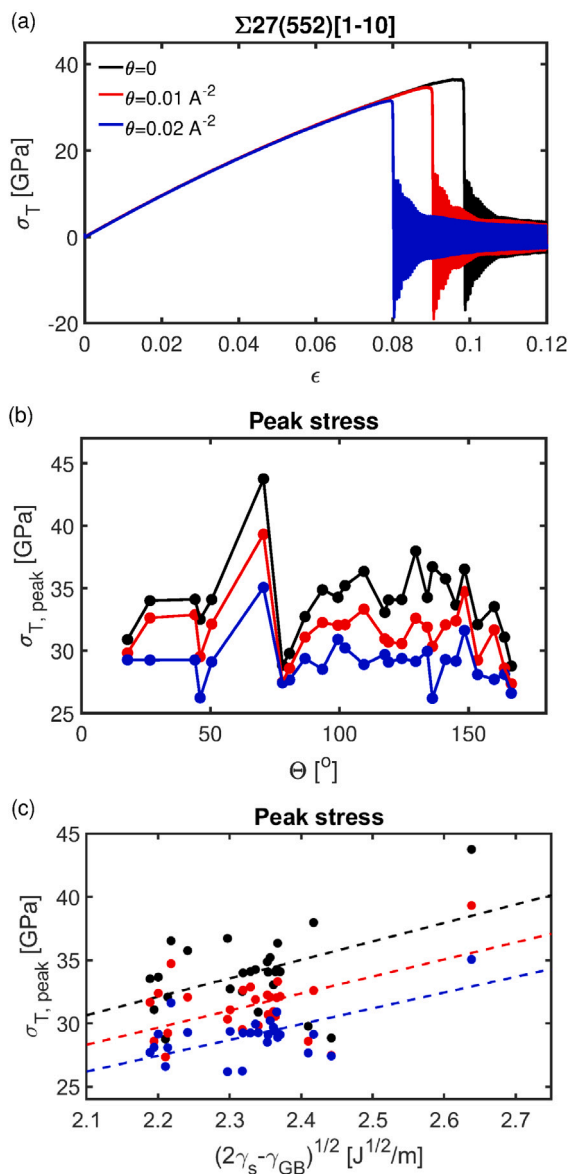
Fig. 10. (a) Stress vs. strain curves for the $\Sigma 27(552)[1\bar{1}0]$ GB for different degrees of impurity coverage. The post-cleavage oscillations are attributed to wave propagation that emerges as a result of recoiling upon failure. Effect of impurity coverage on the peak stress associated with brittle failure: (b) peak stress as function of misorientation angle and (c) as function of the ideal energy release rate. In (c) the dashed lines indicate a linear fit between the peak stress and the square root of the energy release rate.

a fitting strategy to reproduce the work of separation of impurity inhabited GBs as derived from DFT. Outcomes from the classical tensile modelling indicate that the P-impurities have an embritteling effect — even for the relatively low degrees of impurity coverage considered herein. This manifests in suppression of ductile mechanisms in preference of cleavage, as indicated in Table 4, and reduction in GB strength associated with cleavage, see Fig. 10.

The fact that the fractured surfaces are typically decorated with P atoms is an indication that the P atom sites are bond weakening sites in the GB proximity, at which decohesion originates. This is in line with our previous DFT investigation, which revealed charge transfer from W to P in the GB proximity [22]. Such behaviour causes the formation of negatively charged ions, which in agreement with predictions of the unified theory of Cottrell [86] promotes screening across the interface. These tendencies concur with several previous DFT investigations [18–21], where it has been reported that P impurities yield reduced work

of separation of GBs. Although the 2NN-MEAM formalism does not explicitly account for charge transfer, its screening effects can be captured by ensuring low nearest neighbour bond strength for the W–P pair and notable second nearest neighbour screening, via the screening parameters C_{min}(W–P–W) and C_{max}(W–P–W) associated with the binary potential (see Table 3). Herein, we especially note the high value of C_{max}(W–P–W), which indicates that the screening distance extends relatively far and that the presence of P-impurities has a screening impact on the W–W interaction. Thus, especially in low coordinated environments, such as GBs, the potential is anticipated to promote bond weakening, which causes reduced ductility and GB strength.

Notably, it is seen that for the $\Sigma 27(552)[\bar{1}10]$ GB, our classical modelling predicts reduced peak stress and work of separation, see Fig. 10(a). These results are in contrast to previous DFT findings [18], for which the cohesion of the $\Sigma 27$ GB was reported to improve. A possible explanation for such unexpected outcomes from DFT was put forward by Scheiber [51], in which it was argued that the selection of predefined fracture plane is key, such that it corresponds to the lowest work of separation. This is likely the main cause for the reported counter-intuitive behaviour in [18], which indicates that the new potential captures the GB embritteling behaviour for the binary W–P system.

Compared with experimental observations, the atomistic modelling captures the previously reported embritteling tendencies connected with P-impurity segregation [2,16,17]. But it is emphasized that change in behaviour – from ductile to brittle – on most accounts occurs already at lower concentrations than reported in the literature. Such discrepancies are attributed to the inability of most previously adopted techniques, e.g. fractographic analysis or impact testing in tandem with Auger spectroscopy, to resolve the occurrence or suppression of highly localized atomic-scale plasticity mechanisms, or to quantify the strength of individual GBs.

6. Summary and conclusions

In the present work we have generated a new 2NN-MEAM potential for the binary W–P system and investigated the impact of P-impurities on the GB strength in tungsten. By adopting a fitting strategy that incorporates the impurity-induced reduction in work of separation of a GB as part of the fitting database, we have produced a potential that at least qualitatively captures the GB embritteling behaviour predicted by DFT.

Classical tensile modelling of individual GBs indicate that the presence of P promotes embrittlement by the reduced GB strength, which favours brittle cleavage as the dominating failure mechanism. Thus, P atoms act as screening impurities that weaken and reduce the strength of GBs. These results concur with experimental observations in the literature where a correlation between the P content and reduced ductility has been reported. Moreover, this is in line previous DFT results [22], where charge transfer cause the formation of negatively charged P ions that screen the interaction across the GB interface. Although attempts to correlate the peak stress with the ideal energy release rate were made, only rough predictive trends between the two could be extracted, which suggest an averaged decrease of 4.5 GPa in the peak stress is obtained for the considered range of impurity coverage.

CRediT authorship contribution statement

Pär A.T. Olsson: Conceptualization, Methodology, Investigation, Potential fitting and evaluation, DFT modelling, MD modelling (potential evaluation), Formal analysis, Writing – original draft, Review and editing, Funding acquisition. **Praveenkumar Hiremath:** Methodology, MD modelling (GB decohesion modelling), Analysis, Writing – original draft, Review and editing. **Solveig Melin:** Writing – review and editing.

Declaration of competing interest

The authors declare that they have no known competing financial interests or personal relationships that could have appeared to influence the work reported in this paper.

Data availability

The MEAM potential files for LAMMPS are available as part of the supplementary material. The data required to reproduce these findings will be provided by the corresponding author upon reasonable request.

Appendix A. *Ab initio* database generation

A.1. Numerical details

To parametrize and evaluate the potential we relied on data derived from DFT modelling. To this end we used the Vienna *ab initio* simulation package (VASP) [87–90]. The interaction between valence electrons and the core were described using standard pseudopotentials from the VASP library, generated with the projector augmented-wave (PAW) method [91,92]. The electronic valence configurations were $5d^4 6s^2$ (W) and $3s^2 3p^3$ (P) and the exchange–correlation functional was described within the generalized gradient approximation using the Perdew–Burke–Ernzerhof (PBE) formula [93,94].

We converged the kinetic energy cutoff for the plane-wave basis set and the k-point density such that the ground state was converged within 1.0 meV/atom. To this end we utilized a $16 \times 16 \times 16$ k-point grid for the tungsten primitive BCC cell generated using the Monkhorst–Pack method [95] and a cutoff of 400 eV. The adopted k-point meshes for other supercells were made commensurate with the primitive BCC cell. To facilitate the Brillouin zone integration we used smearing based on the Methfessel–Paxton scheme [96] with a smearing width of 0.2 eV.

A.2. Dataset generation

To compute the substitutional defect formation energy we performed fully relaxed calculations, i.e. with both coordinate and fully anisotropic supercell relaxations. The considered geometry was a 128 atom supercell, which was sufficiently large to yield well-converged results. For consistency, the classical calculations were performed using an identical setup. The point defect formation energy was computed as

$$E_f = E_{W+P} - (N E_{b,W} + E_{b,P}) \tag{A.1}$$

where E_{W+P} represents the ground state energy for the system containing the point defect, $E_{b,W}$ and N are the bulk cohesive energy for tungsten and the number of W particles in setup, while $E_{b,P}$ is the reference energy for P. When computing the target energies we utilized the reference phase, i.e. BCC, as ground state.

The RGS calculations were performed using two different GBs: $\Sigma 3(112)[\bar{1}10]$ and $\Sigma 5(013)[100]$. Their respective dimensions were $9.0 \times 5.5 \times 31.3$ Å^3 and $6.3 \times 10.0 \times 20.7$ Å^3, such that they contained 96 and 80 atoms, respectively. The impurities were positioned at the centre of the GBs as indicated in Fig. 2 such that the coverage corresponded

to $\theta \leq 0.04$ Å^{-2}. The traction, σ, was calculated by differentiating the energy–separation function, $\phi(\delta)$, with respect to the separation, δ, as

$$\sigma(\delta) = \frac{1}{A} \frac{d\phi}{d\delta}, \tag{A.2}$$

where A is the cross-sectional area of the crystal.

Appendix B. Supplementary data

Supplementary material related to this article can be found online at https://doi.org/10.1016/j.commatsci.2023.112017.

References

[1] S.J. Zinkle, Fusion materials science: Overview of challenges and recent progress, Phys. Plasmas 12 (5) (2005) 058101.

[2] B. Gludovatz, S. Wurster, T. Weingärtner, A. Hoffmann, R. Pippan, Influence of impurities on the fracture behaviour of tungsten, Phil. Mag. 91 (22) (2011) 3006–3020.

[3] C. Bonnekoh, U. Jäntsch, J. Hoffmann, H. Leiste, A. Hartmaier, D. Weygand, A. Hoffmann, J. Reiser, The brittle-to-ductile transition in cold rolled tungsten plates: Impact of crystallographic texture, grain size and dislocation density on the transition temperature, Int. J. Refract. Met. H. 78 (2019) 146–163.

[4] M. Rieth, S.L. Dudarev, S.M.G. de Vicente, J. Aktaa, T. Ahlgren, S. Antusch, D. Armstrong, M. Balden, N. Baluc, M.-F. Barthe, W. Basuki, M. Battabyal, C. Becquart, D. Blagoeva, H. Boldyryeva, J. Brinkmann, M. Celino, L. Ciupinski, J. Correia, A.D. Backer, C. Domain, E. Gaganidze, C. Garcia-Rosales, J. Gibson, M. Gilbert, S. Giusepponi, B. Gludovatz, H. Greuner, K. Heinola, T. Höschen, A. Hoffmann, N. Holstein, F. Koch, W. Krauss, H. Li, S. Lindig, J. Linke, C. Linsmeier, P. Lopez-Ruiz, H. Maier, J. Matejicek, T. Mishra, M. Muhammed, A. Munoz, M. Muzyk, K. Nordlund, D. Nguyen-Manh, J. Opschoor, N. Ordas, T. Palacios, G. Pintsuk, R. Pippan, J. Reiser, J. Riesch, S.G. Roberts, L. Romaner, M. Rosinski, M. Sanchez, W. Schulmeyer, H. Traxler, A. Urena, J. van der Laan, L. Veleva, S. Wahlberg, M. Walter, T. Weber, T. Weitkamp, S. Wurster, M.A. Yar, J.H. You, A. Zivelonghi, Recent progress in research on tungsten materials for nuclear fusion applications in Europe, J. Nucl. Mater. 432 (2013) 482–500.

[5] V. Philipps, Tungsten as material for plasma-facing components in fusion devices, J. Nucl. Mater. 415 (2011) S2 – S9.

[6] A. Giannattasio, S.G. Roberts, Strain-rate dependence of the brittle-to-ductile transition temperature in tungsten, Phil. Mag. 87 (17) (2007) 2589–2598.

[7] E. Gaganidze, D. Rupp, J. Aktaa, Fracture behaviour of polycrystalline tungsten, J. Nucl. Mater. 446 (1) (2014) 240–245.

[8] M. Wirtz, I. Uytdenhouwen, V. Barabash, F. Escourbiac, T. Hirai, J. Linke, T. Loewenhoff, S. Panayotis, G. Pintsuk, Material properties and their influence on the behaviour of tungsten as plasma facing material, Nucl. Fusion 57 (6) (2017) 066018.

[9] A. Giannattasio, Z. Yao, E. Tarleton, S. Roberts, Brittle-ductile transitions in polycrystalline tungsten, Phil. Mag. 90 (30) (2010) 3947–3959.

[10] Y. Zhang, A.V. Ganeev, J.T. Wang, J.Q. Liu, I.V. Alexandrov, Observations on the ductile-to-brittle transition in ultrafine-grained tungsten of commercial purity, Mater. Sci. Eng. A 503 (1) (2009) 37–40.

[11] B.G. Butler, J.D. Paramore, J.P. Ligda, C. Ren, Z.Z. Fang, S.C. Middlemas, K.J. Hemker, Mechanisms of deformation and ductility in tungsten – A review, Int. J. Refract. Hard Met. 75 (2018) 248–261.

[12] T. Hirai, S. Carpentier-Chouchana, F. Escourbiac, S. Panayotis, A. Durocher, L. Ferrand, M. Garcia-Martinez, J. Gunn, V. Komarov, M. Merola, R. Pitts, G. De Temmerman, Design optimization of the ITER tungsten divertor vertical targets, Fusion Eng. Des. 127 (2018) 66–72.

[13] S. Panayotis, T. Hirai, V. Barabash, A. Durocher, F. Escourbiac, J. Linke, T. Loewenhoff, M. Merola, G. Pintsuk, I. Uytdenhouwen, M. Wirtz, Self-castellation of tungsten monoblock under high heat flux loading and impact of material properties, Nucl. Mater. Energy 12 (2017) 200–204.

[14] Y. Huang, M. Tillack, N. Ghoniem, Tungsten monoblock concepts for the fusion nuclear science facility (FNSF) first wall and divertor, Fusion Eng. Des. 135 (2018) 346–355.

[15] M. Oude Vrielink, J. van Dommelen, M. Geers, Multi-scale fracture probability analysis of tungsten monoblocks under fusion conditions, Nucl. Mater. Energy 28 (2021) 101032.

[16] T.H. Loi, J.P. Morniroli, M. Gantois, Brittle fracture of polycrystalline tungsten, J. Mater. Sci. 20 (1985) 199–206.

[17] A. Joshi, D.F. Stein, Intergranular brittleness studies in tungsten using auger spectroscopy, Metall. Trans. 1 (9) (1970) 2543.

[18] W. Setyawan, R.J. Kurtz, Effects of B, C, N, O, P and S Impurities on Tungsten $\Sigma 27[110]\{552\}$ and $\Sigma 3[110]\{112\}$ Grain Boundaries, Fusion Reactor Materials Program Report, 53, Oak Ridge National Laboratory - MST Division, 2012, p. 64.

[19] G.L. Krasko, Effect of impurities on the electronic structure of grain boundaries and intergranular cohesion in tungsten, Int. J. Refract. Met. H. 12 (5) (1993) 251–260.

[20] Z. Pan, L.J. Kecskes, Q. Wei, The nature behind the preferentially embrittling effect of impurities on the ductility of tungsten, Comput. Mater. Sci. 93 (2014) 104–111.

[21] D. Scheiber, R. Pippan, P. Puschnig, L. Romaner, Ab initio search for cohesion-enhancing impurity elements at grain boundaries in molybdenum and tungsten, Model. Simul. Mater. Sci. Engng. 24 (8) (2016) 085009.

[22] P.A.T. Olsson, J. Blomqvist, Intergranular fracture of tungsten containing phosphorus impurities: A first principles investigation, Comput. Mater. Sci. 139 (2017) 368–378.

[23] W. Setyawan, R.J. Kurtz, Ab initio study of H, He, Li and Be impurity effect in tungsten $\Sigma 3\{112\}$ and $\Sigma 27\{552\}$ grain boundaries, J. Phys.: Condens. Matter 26 (13) (2014) 135004.

[24] W. Setyawan, R.J. Kurtz, Effects of transition metals on the grain boundary cohesion in tungsten, Scr. Mater. 66 (8) (2012) 558–561.

[25] D. Scheiber, R. Pippan, P. Puschnig, L. Romaner, Ab initio calculations of grain boundaries in BCC metals, Model. Simul. Mater. Sci. Engng. 24 (3) (2016) 035013.

[26] D. Scheiber, R. Pippan, P. Puschnig, A. Ruban, L. Romaner, Ab-initio search for cohesion-enhancing solute elements at grain boundaries in molybdenum and tungsten, Int. J. Refract. Met. H. 60 (2016) 75–81.

[27] M.S. Daw, M.I. Baskes, Semiempirical, quantum mechanical calculation of hydrogen embrittlement in metals, Phys. Rev. Lett. 50 (1983) 1285–1288.

[28] M.S. Daw, M.I. Baskes, Embedded-atom method: Derivation and application to impurities, surfaces, and other defects in metals, Phys. Rev. B 29 (12) (1984) 6443–6453.

[29] M.I. Baskes, Application of the embedded-atom method to covalent materials: A semiempirical potential for silicon, Phys. Rev. Lett. 59 (1987) 2666–2669.

[30] M.I. Baskes, J.S. Nelson, A.F. Wright, Semiempirical modified embedded-atom potentials for silicon and germanium, Phys. Rev. B. 40 (9) (1989) 6085–6100.

[31] M. Baskes, Modified embedded-atom potentials for cubic materials and impurities, Phys. Rev. B. 45 (5) (1992) 2727–2742.

[32] B.-J. Lee, M.I. Baskes, Second nearest-neighbor modified embedded-atom-method potential, Phys. Rev. B 62 (2000) 8564–8567.

[33] B.-J. Lee, M.I. Baskes, H. Kim, Y. Koo Cho, Second nearest-neighbor modified embedded atom method potentials for BCC transition metals, Phys. Rev. B 64 (2001) 184102.

[34] M.I. Baskes, J.E. Angelo, C.L. Bisson, Atomistic calculations of composite interfaces, Model. Simul. Mater. Sci. Engng. 2 (3A) (1994) 505–518.

[35] M. Baskes, Atomistic potentials for the molybdenum–silicon system, Mater. Sci. Engng. A 261 (1) (1999) 165–168.

[36] H.-K. Kim, W.-S. Jung, B.-J. Lee, Modified embedded-atom method interatomic potentials for the Fe–Ti–C and Fe–Ti–N ternary systems, Acta Mater. 57 (11) (2009) 3140–3147.

[37] J.H. Rose, J. Ferrante, J.R. Smith, Universal binding energy curves for metals and bimetallic interfaces, Phys. Rev. Lett. 47 (1981) 675–678.

[38] S.M. Valone, M.I. Baskes, R.L. Martin, Atomistic model of helium bubbles in gallium-stabilized plutonium alloys, Phys. Rev. B 73 (2006) 214209.

[39] G. Bonny, D. Terentyev, A. Bakaev, P. Grigorev, D.V. Neck, Many-body central force potentials for tungsten, Model. Simul. Mater. Sci. Engng. 22 (5) (2014) 053001.

[40] P. Hiremath, S. Melin, E. Bitzek, P.A.T. Olsson, Effects of interatomic potential on fracture behaviour in single- and bicrystalline tungsten, Comput. Mater. Sci. 207 (2022) 111283.

[41] D.-K. Seo, R. Hoffmann, What determines the structures of the group 15 elements? J. Solid State Chem. 147 (1) (1999) 26–37.

[42] U. Häussermann, High-pressure structural trends of group 15 elements: Simple packed structures versus complex host–guest arrangements, Chem. Eur. J. 9 (7) (2003) 1471–1478.

[43] W.-S. Ko, N.J. Kim, B.-J. Lee, Atomistic modeling of an impurity element and a metal-impurity system: Pure P and Fe-P system, J. Condens. Matter Phys. 24 (22) (2012) 225002.

[44] B. Liu, H. Zhang, J. Tao, Z. Liu, X. Chen, Y. Zhang, Development of a second-nearest-neighbor modified embedded atom method potential for silicon–phosphorus binary system, Comput. Mater. Sci. 120 (2016) 1–12.

[45] W.-S. Ko, B.-J. Lee, Origin of unrealistic blunting during atomistic fracture simulations based on MEAM potentials, Phil. Mag. 94 (16) (2014) 1745–1753.

[46] J.A. Nelder, R. Mead, A simplex method for function minimization, Comput. J. 7 (4) (1965) 308–313.

[47] E. Lassner, W.D. Schubert, Tungsten: Properties, Chemistry, Technology of the Element, Alloys, and Chemical Compounds, Springer US, 2012.

[48] H. Jehn, S. Gmünd, G. Bär, E. Best, E. Koch, Reactions with phosphorus, in: J. von Jouanne, E. Koch, E. Koch (Eds.), W Tungsten: Supplement Volume a 5 B Metal, Chemical Reactions with Nonmetals Nitrogen to Arsenic, Springer Berlin Heidelberg, Berlin, Heidelberg, 1993, pp. 191–193.

[49] D. Nguyen-Manh, A.P. Horsfield, S.L. Dudarev, Self-interstitial atom defects in BCC transition metals: Group-specific trends, Phys. Rev. B 73 (2006) 020101.

[50] P.M. Derlet, D. Nguyen-Manh, S.L. Dudarev, Multiscale modeling of crowdion and vacancy defects in body-centered-cubic transition metals, Phys. Rev. B 76 (2007) 054107.

[51] D. Scheiber, Theoretical Study of Grain Boundaries in Tungsten and Molybdenum (Ph.D. Thesis), Karl–Franzens–Universität, Graz, 2016.

[52] E. Toijer, P.A.T. Olsson, P. Olsson, Ab initio modelling of intergranular fracture of nickel containing phosphorus: Interfacial excess properties, Nucl. Mater. Energy 28 (2021) 101055.

[53] O. Nguyen, M. Ortiz, Coarse-graining and renormalization of atomistic binding relations and universal macroscopic cohesive behavior, J. Mech. Phys. Solids 50 (8) (2002) 1727–1741.

[54] P.A.T. Olsson, K. Kese, M. Kroon, A.-M. Alvarez Holston, Ab initio-based fracture toughness estimates and transgranular traction-separation modelling of zirconium hydrides, Modell. Simul. Mater. Sci. Eng. 23 (4) (2015) 045015.

[55] P.A.T. Olsson, M. Mrovec, M. Kroon, First principles characterisation of brittle transgranular fracture of titanium hydrides, Acta Mater. 118 (2016) 362–373.

[56] S. Ranganathan, On the geometry of coincidence-site lattices, Acta Crystal. 21 (2) (1966) 197–199.

[57] R. Hadian, B. Grabowski, J. Neugebauer, GBcode: A grain boundary generation code, J. Open Source Softw. 3 (29) (2018) 900.

[58] B. Sadigh, P. Erhart, A. Stukowski, A. Caro, E. Martinez, L. Zepeda-Ruiz, Scalable parallel Monte Carlo algorithm for atomistic simulations of precipitation in alloys, Phys. Rev. B 85 (18) (2012) 184203.

[59] N. Metropolis, A.W. Rosenbluth, M.N. Rosenbluth, A.H. Teller, E. Teller, Equation of state calculations by fast computing machines, J. Chem. Phys. 21 (6) (1953) 1087–1092.

[60] G. Bhanot, The metropolis algorithm, Rep. Progr. Phys. 51 (3) (1988) 429.

[61] P. Diaconis, L. Saloff-Coste, What do we know about the Metropolis algorithm? J. Comput. System Sci. 57 (1) (1998) 20–36.

[62] I. Beichl, F. Sullivan, The metropolis algorithm, Comput. Sci. Engng. 2 (1) (2000) 65–69.

[63] D.E. Spearot, M.A. Tschopp, K.I. Jacob, D.L. McDowell, Tensile strength of $< 100 >$ and $< 110 >$ tilt bicrystal copper interfaces, Acta Mater. 55 (2) (2007) 705–714.

[64] D.E. Spearot, Evolution of the E structural unit during uniaxial and constrained tensile deformation, Mech. Res. Commun. 35 (1–2) (2008) 81–88.

[65] L. Zhang, C. Lu, K. Tieu, Atomistic simulation of tensile deformation behavior of $\Sigma 5$ tilt grain boundaries in copper bicrystal, Sci. Rep. 4 (1) (2014) 1–9.

[66] L. Zhang, C. Lu, L. Pei, X. Zhao, J. Zhang, K. Tieu, Evaluation of mechanical properties of $\Sigma 5(210)/[001]$ tilt grain boundary with self-interstitial atoms by molecular dynamics simulation, J. Nanomater. 2017 (2017) 1–11.

[67] R. Dingreville, D. Aksoy, D.E. Spearot, A primer on selecting grain boundary sets for comparison of interfacial fracture properties in molecular dynamics simulations, Sci. Rep. 7 (1) (2017) 1–12.

[68] E. Martínez, B.P. Uberuaga, B.D. Wirth, Atomistic modeling of helium segregation to grain boundaries in tungsten and its effect on de-cohesion, Nucl. Fusion 57 (8) (2017) 086044.

[69] J.J. Möller, E. Bitzek, R. Janisch, A. ul Hassan, A. Hartmaier, Fracture ab initio: a force-based scaling law for atomistically informed continuum models, J. Mater. Res. 33 (22) (2018) 3750–3761.

[70] S. Nosé, A unified formulation of the constant temperature molecular dynamics methods, J. Chem. Phys. 81 (1) (1984) 511–519.

[71] S. Nosé, A molecular dynamics method for simulations in the canonical ensemble, Mol. Phys. 52 (2) (1984) 255–268.

[72] W.G. Hoover, Canonical dynamics: Equilibrium phase-space distributions, Phys. Rev. A 31 (3) (1985) 1695.

[73] D.J. Evans, B.L. Holian, The Nose–Hoover thermostat, J. Chem. Phys. 83 (8) (1985) 4069–4074.

[74] A.P. Thompson, S.J. Plimpton, W. Mattson, General formulation of pressure and stress tensor for arbitrary many-body interaction potentials under periodic boundary conditions, J. Chem. Phys. 131 (15) (2009) 154107.

[75] D. Tsai, The virial theorem and stress calculation in molecular dynamics, J. Chem. Phys. 70 (3) (1979) 1375–1382.

[76] S. Plimpton, Fast parallel algorithms for short-range molecular dynamics, J. Comput. Phys. 117 (1995) 1–19.

[77] A.P. Thompson, H.M. Aktulga, R. Berger, D.S. Bolintineanu, W.M. Brown, P.S. Crozier, P.J. in 't Veld, A. Kohlmeyer, S.G. Moore, T.D. Nguyen, R. Shan, M.J. Stevens, J. Tranchida, C. Trott, S.J. Plimpton, LAMMPS - A flexible simulation tool for particle-based materials modeling at the atomic, meso, and continuum scales, Comput. Phys. Comm. 271 (2022) 108171.

[78] A.A. Guzman, J. Jeon, A. Hartmaier, R. Janisch, Hydrogen embrittlement at cleavage planes and grain boundaries in BCC iron: Revisiting the first- principles cohesive zone model, Materials 13 (24) (2020) 5785.

[79] R.C. Ehemann, J.W. Nicklas, H. Park, J.W. Wilkins, Ab initio based empirical potential applied to tungsten at high pressure, Phys. Rev. B 95 (2017) 184101.

[80] A. Stukowski, K. Albe, Extracting dislocations and non-dislocation crystal defects from atomistic simulation data, Model. Simul. Mater. Sci. Engng. 18 (8) (2010) 085001.

[81] A. Stukowski, Visualization and analysis of atomistic simulation data with OVITO–the Open Visualization Tool, Model. Simul. Mater. Sci. Engng. 18 (1) (2009) 015012.

[82] G. Schoeck, L. Romaner, Deviations and polarity of [100] dislocations in BCC metals, Phil. Mag. Lett. 90 (6) (2010) 385–391.

[83] C.R. Weinberger, B.L. Boyce, C.C. Battaile, Slip planes in BCC transition metals, Int. Mater. Rev. 58 (5) (2013) 296–314.

[84] A.A. Griffith, The phenomena of rupture and flow in solids, Philos. Trans. R. Soc. Lond. Ser. A 221 (582–593) (1921) 163–198.

[85] D. Scheiber, O. Renk, M. Popov, L. Romaner, Temperature dependence of surface and grain boundary energies from first principles, Phys. Rev. B 101 (2020) 174103.

[86] A. Cottrell, Unified theory of effects of segregated interstitials on grain boundary cohesion, Mater. Sci. Tech. 6 (9) (1990) 806–810.

[87] G. Kresse, J. Hafner, Ab initio molecular dynamics for liquid metals, Phys. Rev. B 47 (1993) 558–561.

[88] G. Kresse, J. Hafner, Ab initio molecular-dynamics simulation of the liquid-metal amorphous-semiconductor transition in germanium, Phys. Rev. B 49 (1994) 14251–14269.

[89] G. Kresse, J. Furthmüller, Efficient iterative schemes for ab initio total-energy calculations using a plane-wave basis set, Phys. Rev. B 54 (1996) 11169–11186.

[90] G. Kresse, J. Furthmüller, Efficiency of ab-initio total energy calculations for metals and semiconductors using a plane-wave basis set, Comput. Mater. Sci. 6 (1) (1996) 15–50.

[91] P.E. Blöchl, Projector augmented-wave method, Phys. Rev. B 50 (1994) 17953–17979.

[92] G. Kresse, D. Joubert, From ultrasoft pseudopotentials to the projector augmented-wave method, Phys. Rev. B 59 (1999) 1758–1775.

[93] J.P. Perdew, K. Burke, M. Ernzerhof, Generalized gradient approximation made simple, Phys. Rev. Lett. 77 (1996) 3865–3868.

[94] J.P. Perdew, K. Burke, M. Ernzerhof, Generalized gradient approximation made simple [Erratum], Phys. Rev. Lett. 78 (1997) 1396.

[95] H.J. Monkhorst, J.D. Pack, Special points for Brillouin-zone integrations, Phys. Rev. B 13 (1976) 5188–5192.

[96] M. Methfessel, A.T. Paxton, High-precision sampling for Brillouin-zone integration in metals, Phys. Rev. B 40 (1989) 3616–3621.